Two-dimensional model of a capacitively coupled rf discharge and comparisons with experiments in the Gaseous Electronics Conference reference reactor

J. P. Boeuf*,† and L. C. Pitchford*
JILA, University of Colorado, Boulder, Colorado 80309-0440
(Received 22 August 1994)

We present results from a two-dimensional (2D) numerical fluid model of rf discharges in conditions close to recently published measurements of the spatial distribution of plasma density in the Gaseous Electronic Conference reference cell. The discharge is in pure argon at pressures in the 100 mtorr range, frequency 13.56 MHz, and rf voltage amplitudes on the order of 100 V. The model is based on solutions of the continuity, momentum (drift-diffusion), and energy equations for the electrons, continuity, and drift-diffusion equation for positive ions, coupled with the Poisson equation. The results of the model are qualitatively and quantitatively in good agreement with the experiments. The model predicts a maximum of plasma density off axis, as in the experiment. The ion current density on the electrode is also nonuniform, and increases radially in the conditions of the experiments. The effects of the rf voltage, pressure, and reactor geometry (electrode dimensions, gap length, guard rings, etc.) on the plasma properties and on the uniformity of the ion current on the powered electrode are also discussed. It is shown that the existence of a maximum of plasma density in the radial direction, in the conditions of the experiment, is due to the small value of the electrode spacing. The results show that the harmonic content of the discharge current is also geometry dependent. The comparisons show that 2D, three-moment fluid models can accurately describe the discharge and the effects of the chamber geometry on the plasma properties for pressure above the limit where collisionless electron heating does not play a significant role.

PACS number(s): 52.65.−y, 52.80.Pi

I. INTRODUCTION

The Gaseous Electronics Conference reactor [1] (GEC reactor) has been designed to facilitate comparison between experiments performed by different groups in similar rf discharge conditions and to improve the methods of measurement. These experiments are also extremely useful in providing a set of reliable data for modeling and for testing the accuracy of different types of numerical models of capacitively coupled rf discharges. In this paper, we concentrate on the recently published experimental results of Overzet and Hopkins [2,3], where accurate electron-density measurements using Langmuir probe and microwave interferometer techniques have been performed in a GEC reactor in argon, at pressures ranging from 100 to 500 mtorr. In Ref. [3], Overzet and Hopkins present two-dimensional (2D) measurements of the spatial variations of the plasma density in the GEC reactor. The primary goal of the present paper is to compare results from a 2D fluid model of the discharge with the measurements of Ref. [3], and to use the model to help interpret the measurements. In a second part of the paper, we study the effects of rf voltage, pressure, and reactor geometry on the discharge properties, and especially on the radial uniformity of the plasma density and ion current to the left electrode. The ion current density profile on the driven electrode is an important parameter in processing applications, since the uniformity of the process, deposition or etching, is directly related to this parameter.

After the first numerical models of dc discharges by Ward [4,5] more than 30 years ago, the need for accurate descriptions and predictions of dc and rf glow discharges has constantly increased due, to a large extent, to the development of plasma processing in the microelectronics industry. A number of 1D fluid models of dc and rf discharges have been developed in the last ten years [6–28]. Some 2D calculations have also been done more recently [29–38]. These models are fluid models, i.e., are based on a fluid representation of the charged particles, where the first two or three moments of the Boltzmann equation, with appropriate closure relations are used to describe the charged particle transport. These equations are coupled with Poisson's equation, and the model gives the space and time variations of the average properties of the charged particles (density, mean velocity, energy, ionization rate) and of the electric potential.

More detailed (and more time consuming) particle models, where a fully kinetic description of the charged particle transport is used, have also been developed in 1D [39–48] and very recently in 2D [49]. These models (PIC-MCC) use the particle-in-cell technique for the transport of electrons and ions, and Poisson equation, coupled with a Monte Carlo simulation to describe the

*Permanent address: Centre de Physique Atomique de Toulouse (CNRS URA 277), Université Paul Sabatier, 118, route de Narbonne, 31062 Toulouse Cedex, France.
†Electronic address: jbp@cpa01.ups-tlse.fr

collisions between charged particles and neutral atoms or molecules. Since no approximations concerning the transport of electrons and ions are made in the PIC-MCC models, they are accurate in a wider range of discharge conditions (lower pressure, higher frequencies) than the fluid models where assumptions of the charged particle velocity distribution functions must be made in order to close the system of moment equations. Hybrid models, where the high energy part of the electron distribution function is described with a particle simulation while fluid equations are used for the bulk, have also been developed [50–53].

Although PIC-MCC simulations should be used at very low pressure (typically below 100 mtorr), when collisionless heating of the electrons in the sheath becomes important, fluid models have been extremely useful in helping to understand the basic properties of rf [6,7,9,11,13,36,37], dc [15,20,29], and pulsed discharges [54] and in predicting the trends. Hybrid models have also proved to be extremely useful in providing a better understanding of transient [50] and dc [53] discharges. Most of the discharge properties that had been predicted by fluid models have been later verified by PIC-MCC models (compare, for example, Refs. [13] and [48]). Comparisons of the results obtained by different groups having different numerical methods but using the same set of cross sections or swarm parameters and boundary conditions have been compiled by Surendra [55]. These results show that fluid models, although less reliable than fully kinetic models, give reasonably accurate predictions of the discharge properties for sufficiently high pressure. The 2D fluid models of Refs. [36] and [37] have also shown the ability of the models to predict, at least qualitatively, the effect of the electrode configuration on the localization of potential traps in dusty plasmas [56].

As a result of the GEC reference reactor initiative, the recent availability of systematic and careful measurements of electrical characteristics and plasma properties of rf discharges makes it possible to check the validity of the models from a more quantitative point of view.

We present, in Sec. II, the principles of the 2D model and the data that have been used in the calculations. The results of the models, in the conditions of the experiments of Overzet and Hopkins [3], are presented in Sec. III, and compared with the measurements. In Sec. IV, we present a parametric numerical study of the GEC reference reactor in argon, with emphasis on the questions of radial uniformity of plasma density and ion current density on the left electrode.

II. DESCRIPTION OF THE MODEL

The fluid model is the same as the one used by Boeuf, Belenguer, and Hbid [36]. Since the details of the equations and approximations were not given in Ref. [36], a complete description of the model is given in this section. A summary of the model assumptions is given in II A, the equations are listed in II B, a discussion of the assumptions on the ionization and energy loss rates is given in Sec. II C, the boundary conditions are presented in II D, the data used in the simulation are described in II E, and the numerical model is briefly presented in II F.

A. Assumptions of the model

In this paper we only consider the cold gas approximation, i.e., we neglect the interactions between the charged particles and neutral atoms in excited states. The effects of superelastic collisions or stepwise excitation or ionization are therefore neglected. Although these collisions have been shown to play a role in rf discharges at 1 torr in argon [24], we believe that they are not very important in the low pressure conditions (100–250 mtorr) and low rf voltages (amplitude 100 V) of the experiments of Overzet and Hopkins [3]. Only electron impact ionization from the ground state will be considered in the following. Electron-electron and electron-ion collisions are not taken into account in the model (the degree of ionization is on the order of 10^{-6}). Electron-ion recombination is also neglected, which is a good approximation at these low pressures.

Ion transport is described by a continuity equation and a drift-diffusion momentum transport equation. Ion inertia is thus neglected. The model could be slightly improved by using an effective field in the ion drift-diffusion equation to account for ion inertia, as in Refs. [9,11,27,34,35,38].

Electron transport is described by the first three moments of the Boltzmann equation, the continuity, momentum transport and energy transport equation. Inertia terms are also neglected in the electron momentum transport equation, which reduces to the drift-diffusion form (energy gradient terms are neglected in this equation). The electron diffusion coefficient D_e and mobility μ_e are supposed to satisfy the Einstein relation $D_e/\mu_e=(k_B T_e)/e=\frac{2}{3}\varepsilon_e/e$, where the electron temperature T_e or mean energy $\varepsilon_e=\frac{3}{2}k_B T_e$ at each location and time are deduced from the electron energy equation. In order to close the system of electron moment equations we also assume that (1) the pressure tensor is isotropic and diagonal, (2) the drift energy is negligible with respect to the thermal energy, (3) the heat flux is proportional to the electron temperature gradient, (4) the mean electron-neutral collision rates depend only on the electron mean energy. However, the electron distribution function is not supposed to be Maxwellian. The functional dependence of the ionization rate, momentum transfer rate (and mobility), and energy loss rate on the mean energy are supposed to be the same as at equilibrium, in a swarm experiment, as in Richards, Thompson, and Sawin [9]. This assumption is further discussed in Sec. II C. The model supposes cylindrical symmetry.

B. Equations

The following notations are used below. Indices e and p refer to electrons and positive ions, respectively. $n_{e(,p)}(\mathbf{r},t)$ are the electron (ion) number densities at position $\mathbf{r}$ and time t. Since we assume cylindrical symmetry, $\mathbf{r}$ is defined by only two parameters, the axial position x and the radial position ρ. $\mathbf{v}_{e(,p)}$ is the electron (ion) mean velocity, ε_e the electron mean energy, k_i the electron impact ionization rate, $\mu_{e,p}$ and $D_{e,p}$ the charged particle mobilities and diffusion coefficients, and k_L the energy

loss rate. All these parameters are functions of $\mathbf{r}$ and t, with k_i, k_L, μ_e, and D_e depending on $\mathbf{r}$ and t through $\varepsilon_e(r,t)$. $E(\mathbf{r},t)$ is the electric field and $V(\mathbf{r},t)$ the electric potential in the discharge. N is the gas density. Using this notation and the assumptions described in II A, the charged particles transport equations can be written as follows. Positive ions:

$$\frac{\partial n_p}{\partial t}+\nabla\cdot(n_p\mathbf{v}_p)=n_eNk_i \ , \tag{1}$$

$$n_p\mathbf{v}_p=n_p\mu_p\mathbf{E}-D_p\nabla n_p \ ; \tag{2}$$

electrons:

$$\frac{\partial n_e}{\partial t}+\nabla\cdot(n_e\mathbf{v}_e)=n_eNk_i \ , \tag{3}$$

$$n_e\mathbf{v}_e=-n_e\mu_e\mathbf{E}-D_e\nabla n_e \ , \tag{4}$$

$$\frac{\partial n_e\varepsilon_e}{\partial t}+\nabla\cdot(\tfrac{5}{3}n_e\varepsilon_e\mathbf{v}_e+\mathbf{q}_e)=-en_e\mathbf{v}_e\cdot\mathbf{E}-n_eNk_L \ , \tag{5}$$

where the heat flux $\mathbf{q}_e$ is given by

$$\mathbf{q}_e=-\tfrac{2}{3}\kappa\nabla\varepsilon_e, \quad \kappa=\tfrac{5}{2}n_eD_e \tag{6}$$

and

$$\mathbf{E}=-\nabla V \ . \tag{7}$$

The electric potential V is obtained from Poisson's equation,

$$\Delta V=-\frac{e}{\varepsilon_0}(n_p-n_e). \tag{8}$$

The set of equations above is similar to the system used in a number of papers on rf discharge modeling. However, different ways of estimating the ionization, momentum transfer, and energy loss rates have been used in these papers. This question is discussed in Sec. II C. In the present paper, we assume that these rates depend on the mean electron energy in the same way as they do under equilibrium conditions. By "equilibrium conditions" we mean a situation where the rate of electron energy gain is locally balanced by the energy loss rate. The model will therefore give exact results when applied to the conditions of a swarm experiment (uniform electric field, far from boundaries). At equilibrium, all the electron mean properties can be expressed as a function of E/N. Since the electron mean energy ε_e is an increasing function of E/N, all the other electron mean properties can be expressed as a function of ε_e. In the present work, the energy loss rate at equilibrium is obtained by writing that energy gain is locally balanced by energy loss in Eq. (5), i.e., by setting the time and space derivatives to zero. Assume that, at equilibrium, ε_e and μ_e are related to E/N by

$$\varepsilon_e=F(E/N) \tag{9}$$

and

$$\mu_e=\frac{1}{N}G(E/N) \ . \tag{10}$$

Equating the right-hand side of (5) to zero at equilibrium gives the functional dependence of k_L with ε_e:

$$k_L\{\varepsilon_e\}=e\frac{1}{N}(\mu_eE^2)_{\text{equil}}=eG[F^{-1}\{\varepsilon_e\}](F^{-1}\{\varepsilon_e\})^2 \ . \tag{11}$$

Knowing the variation of the ionization rate k_i (from Boltzmann calculations, or from swarm experiments) with E/N at equilibrium,

$$k_i=H(E/N) \ , \tag{12}$$

the functional dependence of k_i with ε_e is given by

$$k_i\{\varepsilon_e\}=H[F^{-1}\{\varepsilon_e\}] \ . \tag{13}$$

The mobility μ_e [and momentum transfer rate $k_m=e/(mN\mu_e)$] can be expressed as a function of the mean electron energy in the same way, using Eqs. (9) and (10):

$$\mu_e=\frac{1}{N}G[F^{-1}\{\varepsilon_e\}] \ . \tag{14}$$

In summary, k_i, μ_e, and k_L in Eqs. (3)–(5) are obtained as follows: (1) the equilibrium functions F, G, H, characterizing the variations with E/N of the mean electron energy, mobility, and ionization rate at equilibrium (constant electric field) must first be tabulated (they can be obtained from a Boltzmann or Monte Carlo code, or from swarm experiments); (2) k_L, k_i, and μ_e at a given location and time during the simulation depend on the electron mean energy at this location and time as indicated in equations (11), (13), and (14), respectively.

Note, finally, that by setting the right-hand side of Eq. (5) to zero at equilibrium, one neglects a term of the order of ε_eNk_i (which would come from the spatial gradient in a steady state swarm experiment). This approximation is reasonable if the electron mean energy is smaller than the ionization threshold, which is generally the case in our conditions (otherwise, it is easy to add this term in the above derivation of k_L [22]).

C. Comments on the ionization and energy loss rates

Different ways of estimating the ionization rate k_i and energy loss rate k_L have been used in rf discharge modeling. The method described in Sec. II B and used in Ref. [36] is similar to the methods used by Richards, Thompson, and Sawin [9], Gogolides and co-workers [11,22], Oh, Choi, and Choi [16], Meyyappan and Govindan [23], and also Barnes, Colter, and Elta [10], Young and Wu [34], and Economou and co-workers [24,38]. A similar idea is also used by Passchier and Goedheer [35], although the energy loss term in this paper (Eq. (3) of Ref. [35]) neglects inelastic losses other than those due to ionization. The assumption that the ionization rate, momentum transfer and energy loss rate depend on the mean energy has been used for a long time in the theory and modeling of electron transport in semiconductor devices [57–60]. The derivation of the energy loss rate in Sec. II B above is identical to the approximation discussed by

Seeger [58] (see Eq. (4m.6), p. 118 of Ref. [58]). It is also possible to introduce, instead of the energy loss rate k_L and momentum exchange rate k_m defined above, an energy relaxation time τ_ε (see Eq. (4m.7), p. 118 of Ref. [58]): $Nk_L\{\varepsilon_e\}=1/\tau_\varepsilon$, and a momentum relaxation time τ_m defined by $Nk_m\{\varepsilon_e\}=1/\tau_m$, where the energy and momentum relaxation times are also functions of the electron mean energy. This relaxation time formulation, is used explicitly, for example, in Refs. [10], [24], and [34] in the context of rf discharge modeling and in Refs. [59] and [60] in the context of semiconductor device modeling. It is completely equivalent to the method used in the present paper and described in Sec. II B.

In other rf discharge models [6,8], the ionization rate and energy loss rate are assumed to be of the Arrhenius form, i.e., proportional to $\exp(-E_i/k_BT_e)$, where E_i is the ionization energy threshold. Meyyappan and Krevkosky [17] assume that the electron distribution function is Maxwellian and obtain an analytical expression of the ionization rate as a function of electron temperature (the ionization cross section is supposed to be constant above the threshold).

Makabe and co-workers [12,21,28] assume that the ionization rate is a function of a reduced effective field $E_{\text{eff}}(\mathbf{r},t)/N$. This effective field is obtained from the solution of a differential equation, which is deduced from an energy equation slightly different from (5). Note that the method described in II B is also equivalent to assuming that the ionization rate depends on a reduced effective field, this effective field being defined as the field which, at equilibrium, would give the same mean electron energy as Eq. (5).

Note, finally, that the equilibrium assumption of Refs. [4,5,7,29,34] means that energy gain is locally balanced by the losses so that the left-hand side of Eq. (5) is supposed to be zero at any time or position in the discharge. In that case, the electron mean energy at a given position and time depends only on the value of E/N at that position and time and is simply given by Eq. (9) (no energy equation is needed). This is equivalent to assuming that the energy relaxation time τ_ε defined above tends to zero, or is negligible with respect to the rf cycle duration. For a frequency of 13.56 Mhz, this assumption becomes reasonable for pressures on the order of 1 torr (the exact limit depends on the gas).

The discussion above shows that there is a variety of approximations of the ionization and energy loss rates in the literature and no systematic comparison of the different approaches has been made. We believe that the method described in this paper and first applied by Richards, Thompson, and Sawin [9] to rf discharges is more coherent and reliable than others for situations where secondary electrons emitted by the electrodes do not contribute significantly to the total ionization. If secondary emission plays an important role [13,14], the electrons emitted by the electrodes and accelerated in the sheaths cannot be treated accurately with the energy equation (5). These electrons should rather be described by a modified energy equation accounting for their beam-like nature [14,15,20] or by a hybrid fluid-kinetic simulation as described in Fiala, Pitchford, and Boeuf [53] for dc glow discharges, Bouef and Pitchford [50] for transient discharges, Sato and Tagashira [51] and Sommerer and Kushner [52] in the case of rf discharges.

D. Boundary conditions

The electron flux normal (index n) and directed toward the electrodes or walls is given by (no reflection or secondary emission is considered in the results below)

$$\Gamma_{e,n}=\tfrac{1}{4}n_e v_{e,\text{th}}, \tag{15}$$

where $v_{e,\text{th}}$ is the electron thermal velocity, given by

$$v_{e,\text{th}}=\left[\frac{8k_BT_e}{\pi m_e}\right]^{1/2}. \tag{16}$$

The electron energy flux to the electrodes and walls is set to

$$\mathbf{q}_{e,n}=\tfrac{1}{4}n_e v_{e,\text{th}}(2k_BT_e). \tag{17}$$

The ion flux to the electrodes and walls is supposed to be purely drift when the ion drift velocity is directed to the wall,

$$\Gamma_{p,n}=n_p\mu_p E_n, \tag{18}$$

and is zero otherwise.

In the case of a dielectric wall, the total charge σ per unit surface of the wall is obtained by assuming that electrons and ions recombine instantaneously on the perfectly absorbing boundary. The surface charge is therefore given by integrating

$$\frac{\partial\sigma}{\partial t}=e(|\Gamma_{p,n}|-|\Gamma_{e,n}|). \tag{19}$$

The boundary conditions for Poisson's equation are of the Dirichlet type (potential is imposed) on electrodes or metallic walls, and of the von Neuman type on dielectric walls (perpendicular field E_n is imposed; assuming a perfect dielectric, this field is obtained from the surface charge σ by $E_n=\mathbf{n}\cdot\mathbf{E}=\sigma/\varepsilon_0$, where $\mathbf{n}$ is a unit vector perpendicular to the surface and directed toward the inside of the reactor).

One of the electrodes is grounded, the other being powered through a capacitor (see Fig. 2). The dc self-bias is obtained iteratively, as in Passchier and Goedheer [35], in such a way that the ion current to the electrode is exactly balanced by the electron current over one rf cycle when harmonic steady state is reached.

E. Data

The data used in the simulation are (1) the electron mean energy, electron mobility, and ionization rate as a function of E/N under equilibrium conditions (functions F, G, H defined in Sec. II B, and (2), the ion mobility and diffusion coefficient as functions of E/N.

The variations of the electron mean energy as a function of E/N (function F) have been obtained using the multiterm Boltzmann solver of Segur, Yousfi, and Bordage [61], the set of electron-neutral cross sections in ar-

gon being the same as in Fiala, Pitchford, and Boeuf [53]. The calculated equilibrium mean energy (function F) is represented in Fig. 1(a). It is about 10% higher than the analytical linear expression used by Richards, Thompson, and Sawin [9] for E/N greater than 10 Td (10^{-16} V cm^2).

The parameters below are given at 300 K. For convenience, the gas pressure p is used instead of the gas density N.

The electron mobility is supposed to be constant and its value is taken from Ward [5]:

$$p\mu_e = 3\times 10^5 \text{ cm}^2\text{ V}^{-1}\text{ s}^{-1}\text{ torr} . \quad (20)$$

The ion mobility is also taken from Ward [5] and is given by

$$p\mu_p = 10^3(1-2.22\times 10^{-3}E/p) \text{ torr cm}^2\text{ V}^{-1}\text{ s}^{-1}$$

$$\text{for } E/p \le 60 \text{ V/(cm torr)} ,$$

$$p\mu_p = \frac{8.25\times 10^3}{\sqrt{E/p}}\left[1-\frac{86.52}{(E/p)^{3/2}}\right] \text{ torr cm}^2\text{ V}^{-1}\text{ s}^{-1}$$

$$\text{for } E/p > 60 \text{ V/(cm torr)} . \quad (21)$$

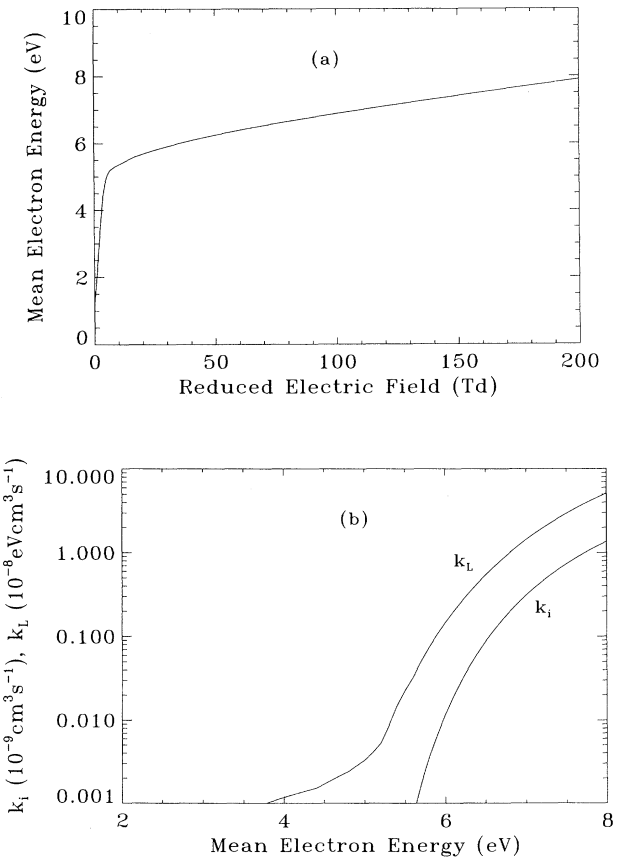

FIG. 1. (a) Mean electron energy as a function of E/N obtained from a multiterm Boltzmann calculation and used in the discharge model [function F of Eq. (9)]; (b) ionization rate k_i and energy loss rate k_L as functions of electron mean energy [Eqs. (13) and (11), respectively].

The ionization rate at equilibrium (function H) is deduced from the ionization coefficient α and mobility by $k_i = (\alpha/N)\mu_e E$. The ionization coefficient at equilibrium is supposed to depend on the reduced electric field according to the formula

$$\alpha/p = A \exp\left\{\frac{-B}{(E/p)^{0.4}}\right\} ,$$

where α is in cm^{-1}, p in torr, and $A = 34$ cm^{-1} and $B = 16$ [V/(cm torr)]$^{0.4}$.

We find that the above formula is in much better agreement with the Boltzmann calculations than the analytical expression of Ward [5].

The electron energy loss rate is obtained from Eq. (11). Ionization rate and energy loss rate are represented in Fig. 1(b) as functions of electron energy. The ion diffusion coefficient is set to 2×10^2 cm^2 s^{-1} at 1 torr, 300 K. The electron diffusion coefficient is deduced from the Einstein relation.

F. Numerical model

As in Refs. [7,29,35,36,50,53], the numerical method is based on the Scharfetter-Gummel [62] discretization scheme of the drift-diffusion equations. In contrast with Refs. [13,14,50,53] the time integration scheme used in this paper is not implicit, i.e., the transport equations and Poisson's equation are integrated successively in time as in Refs. [7,29]. Therefore, no linearization of the system, matrix inversion, and Newton iterations are necessary. Although the explicit method of integration is subject to a constraint on the time integration step (the time step must be smaller than the dielectric relaxation time), we find that for the relatively low plasma density values of the experiments of Overzet and Hopkins [2,3], this constraint is not strong and explicit integration is relatively fast. The time step δt in an explicit integration must satisfy the constraint

$$\delta t < \frac{1}{(e/\varepsilon_0)(n_e\mu_e + n_p\mu_p)} . \quad (22)$$

For a plasma density of 10^9 cm^{-3} in argon at 0.1 torr, this corresponds roughly to $\delta t < 0.2$ ns. At a frequency of 13.56 MHz, the number of time steps per cycle is therefore less than 500. With a fully implicit time integration scheme, this number can be dropped to less than 50 but since the computation cost per time step would be much larger than in the explicit case, the explicit scheme may still be more efficient. The fully implicit scheme is extremely efficient for very large plasma densities [50], or for low frequency or dc discharges [53]. In the model described here, we can use, if necessary and for larger densities, a semi-implicit time integration scheme in order to increase the time step and to accelerate the calculations. In this simple scheme, a prediction of the electron density at time $t+\delta t$, taking into account the field variation during δt, is used in Poisson's equation instead of the electron density at time t, and the constraint defined by Eq. (22) no longer holds (similar ideas are used in Ref. [63]).

The discretization of the electron and ion fluxes [Eqs. (4) and (2)] in our model is identical to Eq. (A7) of Fiala, Pitchford, and Boeuf [53]. Using this discretization, the continuity equations (3) and (1) are expressed as in Eq. (A1) of [53] using a Crank-Nicholson scheme. The continuity equations are integrated in time successively along each spatial direction (splitting technique). Each integration involves the inversion of a simple tridiagonal matrix.

Using Eqs. (4) and (6), the electron energy equation (5) can be modified in the equivalent form:

$$\frac{\partial n_e \varepsilon_e}{\partial t} + \tfrac{5}{3}\nabla\cdot[-n_e\varepsilon_e\mu_e E - D_e\nabla(n_e\varepsilon_e)] = -en_e\mathbf{v}_e\cdot\mathbf{E} - n_e N k_L \ . \quad (23)$$

The left-hand side of this equation has the same form as the left-hand side of the electron continuity equation, the unknown function being here the electron energy density ($n_e\varepsilon_e$) instead of the electron density. The energy flux term $\frac{5}{3}[-n_e\varepsilon_e\mu_e E - D_e\nabla(n_e\varepsilon_e)]$ can therefore be discretized in the same way as the electron flux (Scharfetter-Gummel scheme [62]), and Eq. (23) can be integrated for ($n_e\varepsilon_e$) in the same way as the continuity equation. We have found that if the energy gradient term in the electron momentum transfer equation is not neglected [i.e., if the diffusion term is written $\nabla(n_e D_e)$ instead of $D_e\Delta(n_e)$], the energy equation cannot be written in the form (21) and it is much more delicate to handle numerically.

Poisson's equation is solved at each time step using a successive over relaxation method. The code can deal with relatively complex geometries (the geometry is defined by the user using a simple interactive initialization program), dielectric or metallic walls, in cylindrical or rectangular systems (periodic boundary conditions in the direction perpendicular to the discharge axis can also be used in the rectangular case). It can also be applied to electronegative gases. Accelerating techniques, which will not be described here, can also be used to accelerate convergence toward harmonic steady state (this may be necessary in the case of electronegative gases where the negative ion loss processes that control the density of negative ions can be extremely slow).

For the conditions considered in this paper (typically 13.56 MHz, 0.1 torr argon, plasma density on the order of 10^9 cm^{-3}) the computational time is on the order of a few rf cycles per minute of CPU time on a HP9000/735 workstation. Without acceleration, harmonic steady state (more than 1000 cycles simulated) is reached in less than 10 h CPU time under these conditions. The convergence time can be divided by 10 if one uses accelerating methods (such as overrelaxation of the continuity equation). At steady state, the production-loss balance for each type of particle is checked: the number of electrons (ions) created in the volume per cycle must be equal to the number of electron (ions) lost in the volume (recombination, attachment) and through the walls and electrodes.

III. RESULTS FOR THE GEOMETRY OF THE GEC REFERENCE CELL IN THE CONDITIONS OF OVERZET AND HOPKINS

In this section we show some results of the 2D model described above, for conditions close to the plasma density distribution measurements of Overzet and Hopkins [3], in a GEC reference cell in argon.

A. Conditions of the simulations

The calculations presented below have been performed in pure argon at a gas temperature of 300 K and frequency of 13.56 MHz. The argon pressure has been varied from 0.05 to 0.5 torr, and the amplitude of the rf voltage V_{rf} from 50 to 150 V. The typical reactor geometry is indicated in Fig. 2 (cylindrical symmetry). The powered electrode is surrounded by a grounded guard ring. In all the calculations presented below, the dimensions of the chamber are $X_T = 10$ cm (length) and $R_T = 10$ cm (radius) and the thickness of the guard ring is zero. The grid is uniform axially and radially with 41×41 grid points. The grid spacing is therefore 0.25 cm in both directions.

To simulate the experiments of Overzet and Hopkins [3] in the GEC reference reactor, we used the following electrode dimensions (see Fig. 2):

$R_c = 5$ cm ,

$R_r = 5.25$ cm ,

$R_T = 10$ cm ,

$R_a = 5.25$ cm ,

$X_c = X_r = 3.5$ cm ,

$X_a = 6.25$ cm; $d = X_a - X_c = 2.75$ cm ,

$X_T = 10$ cm .

Note that these dimensions are close but not identical to those of the reactor used by Overzet and Hopkins [3] (in this reactor, d, R_r, R_a, X_T, and R_T were, respectively, 2.54, 5, 5, 12, and 12.5 cm).

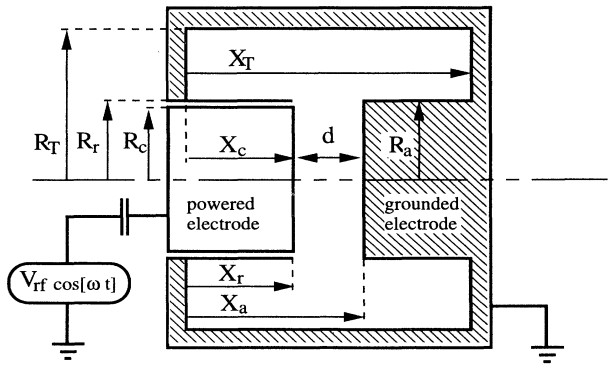

FIG. 2. Geometry of the simulated reactor (GEC reference cell, not to scale).

TABLE I. Definitions of the different discharge conditions simulated and discussed in this paper. Each case is denoted by a number between parentheses, the standard case being (1). Bold characters indicate a change of the corresponding parameter with respect to the standard case.

	V_{rf} (V)	p (torr)	d (cm)	R_c (cm)	R_r (cm)	R_a (cm)	Other
(1)	100	0.1	2.75	5	5.25	5.25	guard ring
(2)	**50**	0.1	2.75	5	5.25	5.25	guard ring
(3)	**150**	0.1	2.75	5	5.25	5.25	guard ring
(4)	100	**0.05**	2.75	5	5.25	5.25	guard ring
(5)	100	**0.25**	2.75	5	5.25	5.25	guard ring
(6)	100	**0.5**	2.75	5	5.25	5.25	guard ring
(7)	100	0.1	**1.5**	5	5.25	5.25	guard ring
(8)	100	0.1	**4**	5	5.25	5.25	guard ring
(9)	100	0.1	**6.5**	5	5.25	5.25	guard ring
(10)	100	0.1	2.75	**3.75**	**4**	**4**	guard ring
(11)	100	0.1	2.75	**7.25**	**7.5**	**7.5**	guard ring
(12)	100	0.1	2.75	5	5.25	**7.25**	guard ring
(13)	100	0.1	2.75	5		5.25	**no guard ring**
(14)	100	0.1	2.75	5		5.25	**no guard ring left plate at cathode potential**

Other cases have also been simulated and are reported in this paper. These cases will be described in Sec. IV. Table I identifies the different cases that have been considered.

B. Description of the results

Figure 3(a) shows the contours of constant electron density $\langle n_e \rangle(x,\rho)$ (averaged over one rf cycle) in the geometrical conditions of Overzet and Hopkins and for $p=0.1$ torr and $V_{rf}=100$ V (200 V peak to peak). One can see an off-axis maximum of the electron density between the two electrodes at the location $x=4.87$ cm and $\rho=3.62$ cm. The radial coordinate of the maximum electron density is slightly smaller than the powered electrode radius. The position of the maximum and its value is in excellent agreement with the measurements of Ref. [3]. Detailed comparisons of the calculations and measurements are given in Sec. III C below. The time averaged plasma potential $\langle V \rangle(x,\rho)$ is shown in Fig. 3(b). The maximum of plasma density is associated, as expected, with a maximum of plasma potential as shown. The potential at the maximum is about 2 V above the potential on axis at the same axial position. The location of these maxima is closer to the powered electrode due to the asymmetry of the reactor. The calculated dc self-bias (average potential of the powered electrode) is -66 V under these conditions. Note that off-axis maxima of the plasma density have been reported in several papers on 2D rf discharge models [32–38]. Experimental probe measurements of the plasma potential in rf discharges [64] have also shown the existence, in some reactor configurations, of off-axis maxima of the plasma potential which are related to plasma density maxima.

The time averaged ionization rate $\langle n_e N k_i \rangle(x,\rho)$ and electron mean energy $\langle \varepsilon_e \rangle(x,\rho)$ are represented in Figs. 4(a) and 4(b), respectively. It is interesting to note that both the ionization rate and mean electron energy reach a maximum at a location close (but not identical) to the maximum of electron density. As mentioned in Ref. [36], the maxima of electron density (or potential) and ionization rate are not necessarily coincident.

Figures 5(a) and 5(b) show the contours of constant time averaged electron density and ionization rate, respectively, in the second case described by Overzet and Hopkins in Ref. [3], i.e., for a pressure of 0.25, all the other parameters being the same as in the previous case. The results are very similar to the 0.1 torr case, the electron density maximum being slightly more pronounced at 0.25 torr.

Figures 6(a) and 6(b) show the radial variations of the time averaged electron and positive ion current densities on the driven electrode ($X=X_c$, $0<\rho<R_c$) in the 0.1 torr and 0.25 torr cases, respectively. The ion current density to the electrode is not uniform and increases radially under these conditions. The sharp increase of the current densities on the edge of the electrode is due to the presence of the guard ring which induces a large radial electric field on the edge of the electrode. Note that although the total electron and ion current (averaged over one cycle) to the electrode are identical, the electron and ion current densities are not identical at each point of the electrode surface. The electron current density is smaller than the ion current density in the center of the electrode, while the reverse is true close to the edge of the electrode.

C. Comparisons with experiment

Figure 7 shows comparisons between the model results and the Langmuir probe measurements of Overzet and Hopkins [3] for a pressure of 0.1 torr. The calculated axial [Fig. 7(a)] and radial [Fig. 7(b)] variations of the aver-

aged electron density are near the electron and ion density measurements of Overzet and Hopkins (see Figs. 1 and 2 of Ref. [3]), which should act [3] as upper and lower bounds of the actual plasma density distribution. The axial and radial shapes of the calculated electron density follows closely the density profiles measured by Overzet and Hopkins. As in the experiment, the peak in the density occurs approximately 1 cm inside of the actual radial edge of the electrodes.

Figure 8 shows the radial profile of the calculated and measured densities for a pressure of 0.25. The agreement between measurements and calculations is also very good in that case.

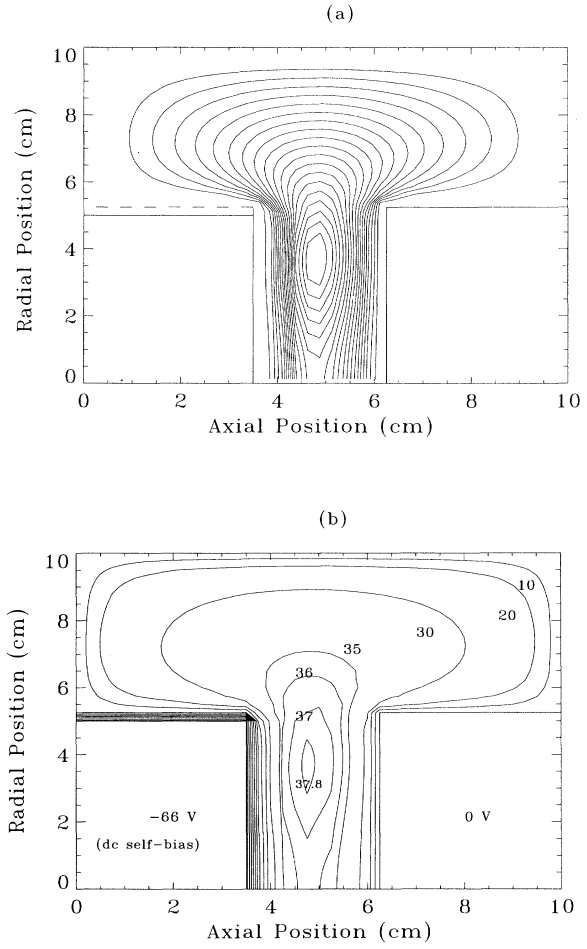

FIG. 3. Contours of constant time averaged (a) electron number density and (b) electric potential in the standard case (1): argon, $V_{rf}=100$ V, $F=13.56$ MHz, $p=0.1$ torr, dimensions approximately equal to the reference cell of Overzet and Hopkins [3]. The increment of the density contours is $\frac{1}{20}$ of the maximum density (2×10^9 cm^{-3}). The increment in the equipotential contours is 10 V, except for the four values below the maximum potential (38.03 V). The dc self-bias of the left electrode is also indicated. The dashed line on the left electrode side represents the guard ring.

IV. OTHER RESULTS AND DISCUSSION

In this section we present a parametric study of the discharge and plasma properties, and discuss the effect of pressure, voltage, and geometry on the radial uniformity of the plasma density, ion current on the left electrode, and other discharge properties. We also briefly comment on the influence of the electrode geometry on the harmonic content of the total discharge current.

A. Conditions of the simulations

The conditions of the simulation results discussed in this section are summarized in Table I. Each set of conditions is noted with a number between parentheses, (1) being the "standard" case of Overzet and Hopkins. In all the simulations, the length of the reactor X_T and its radius R_T have been kept constant (10 cm each). The cathode length X_c is also the same in all simulations ($X_c=3.5$ cm). Note that in most cases, only one of the

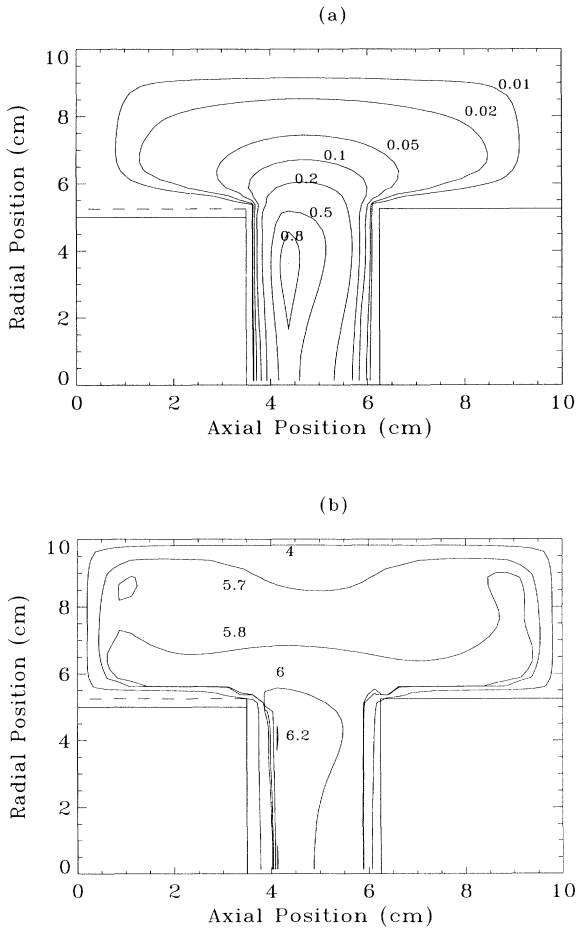

FIG. 4. Contours of constant time averaged (a) ionization rate (unit: 2.5×10^{14} cm^{-3}s^{-1}), and (b) mean electron energy (unit: 1 eV) in the conditions of Fig. 3.

parameters is different from the standard case.

For each case, the parameter that differs from the standard case is printed in bold characters in Table I. This parameter is the rf voltage for cases (2) and (3), the gas pressure for cases (4)–(6), the electrode spacing for cases (7)–(9), the electrode radius for cases (10) and (11), the right electrode radius for case (12). In case (13), the guard ring around the left electrode has been removed. In case (14), the guard ring is also removed, and the plate around the left electrode is no longer grounded and is at the same potential as the powered electrode.

The results at 0.05 torr are probably quantitatively questionable because collisionless heating may be non-negligible at this pressure. The presence of metastable species could also affect the results at 0.5 torr; however, we believe that the trends predicted by the model under these "extreme" conditions are still valid.

B. Parametric study of the off-axis plasma density maximum and ion current density on the powered electrode

The radial variations of the plasma density for different conditions of rf voltage, pressure, electrode spacing, and electrode radius are shown in Fig. 9. We see that the off-axis maximum of plasma density is enhanced by an increase of rf voltage [Fig. 9(a)] or pressure [Fig. 9(b)], everything else being kept constant. An increase in the electrode spacing tends to decrease the importance of the off-axis maximum [Fig. 9(c)]. The radial maximum of plasma density disappears completely when the right electrode is removed [case (9) of table I], i.e., when $X_a = X_T$ (see Fig. 2). This can also be seen in Fig. 10(b), where the contours of constant time averaged electron density corresponding to case (9) are represented. The plasma density is maximum on the discharge axis in that case. The radial maxima of plasma density also decrease and finally disappear when the radius of both electrodes is decreased [Fig. 9(d)].

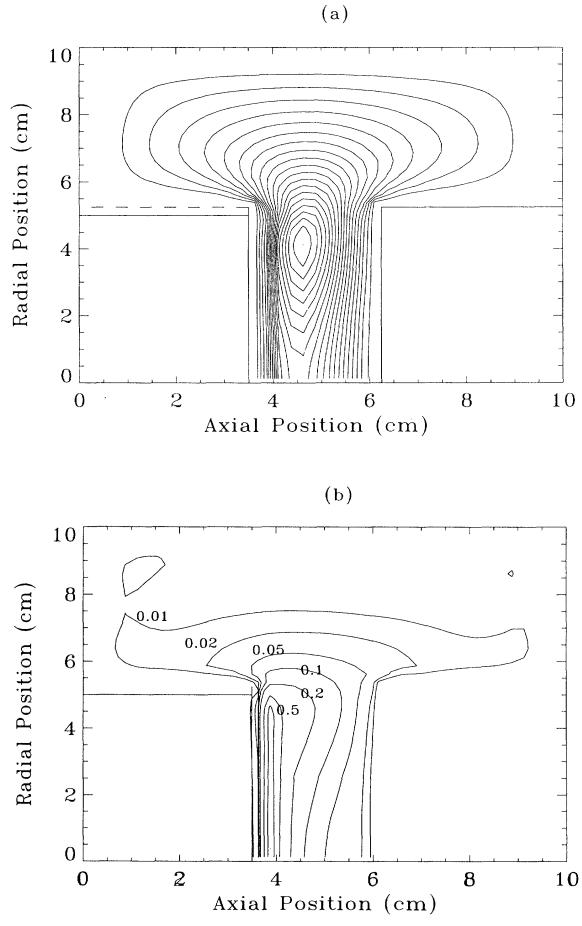

FIG. 5. Contours of constant (a) time averaged electron number density and (b) ionization rate (unit: 7.2×10^{14} cm^{-3} s^{-1}) for a 0.25 torr pressure [case (5)], the other parameters being the same as in Fig. 3. The increment of the density contours is $\frac{1}{20}$ of the maximum density (5.5×10^{9} cm^{-3}).

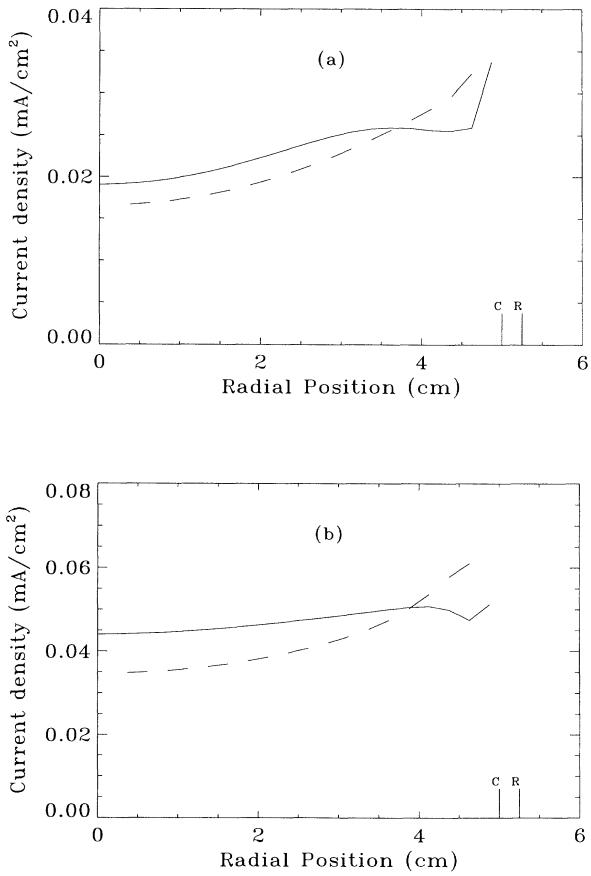

FIG. 6. Electron (dashed line) and ion (solid line) current densities on the surface of the powered electrode for (a) 0.1 torr and (b) 0.25 torr; conditions of Figs. 3 and 5, respectively [cases (1) and (5)].

Increasing the radius of the grounded electrode while keeping constant the driven electrode radius does not affect significantly the existence of the radial nonuniformity, as can be seen in Fig. 10(a), which shows the contours of constant electron number density for case (12).

Taking off the guard ring has a strong effect on the plasma density distribution, as can be seen in Fig. 11(a), where the density contours for case (13) are displayed. The density maximum is now outside the electrode gap, and closer to the driven electrode. This is due to the fact that the lateral part of the driven electrode plays, in that case, an active part in the discharge maintenance, due to the formation of an important sheath field around this electrode. In Fig. 11(a), the plate surrounding the driven electrode is grounded. If this plate is no longer grounded, but, rather, at the same potential as the driven electrode, the shape of electron density contours changes as indicated in Fig. 11(b) [which corresponds to case (13) of Table I]. The plasma density maximum now moves toward the left plate. This is due to the enhanced ionization rate in this region due to the presence of a larger sheath field when this part of the reactor is no longer grounded. Similar effects of the boundary conditions have already been described in Ref. [36].

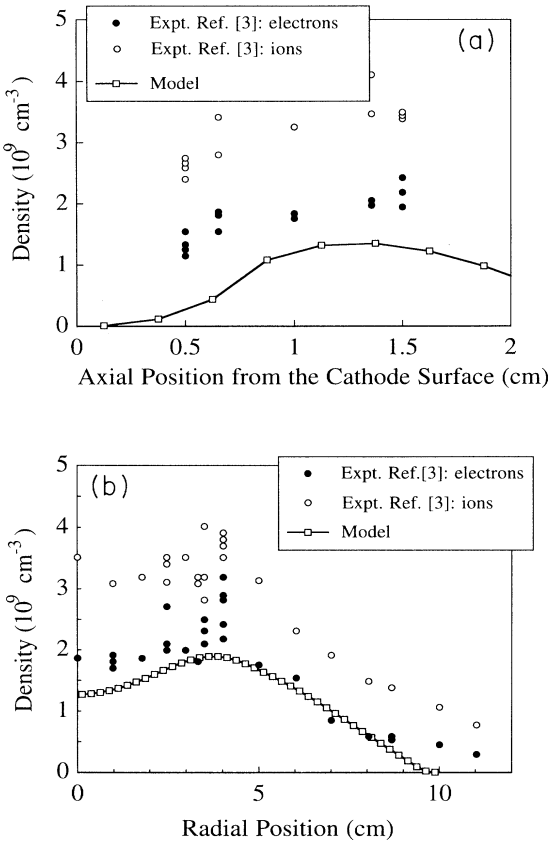

FIG. 7. Comparisons of the calculated (present work) and measured (after Figs. 1 and 2 from Overzet and Hopkins [3]) plasma density (a) on axis and (b) radially, at a distance $x = 1.25$ cm from the surface of the powered electrode at 0.1 torr and 100 V peak rf voltage [case (1)]. The calculated curves (straight lines) correspond to the time averaged electron density of Fig. 3(a). The experimental results correspond to the Langmuir probe measurements of the time averaged electron (●) and ion (○) density. These measurements should act as upper and lower bounds on the actual plasma density [3].

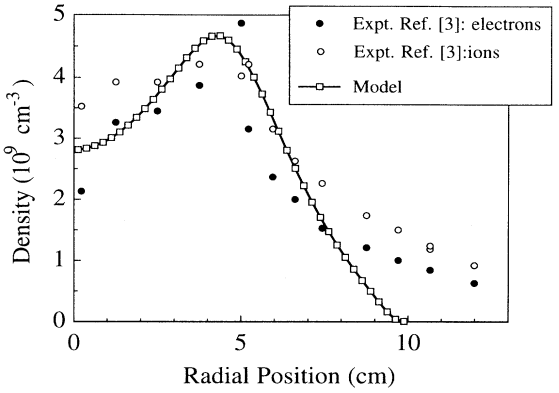

FIG. 8. Comparisons of the calculated (present work) and measured (after Fig. 4 of Overzet and Hopkins [3]) radial profile of the plasma density at a distance $x = 1.25$ cm from the surface of the powered electrode at 0.25 torr and 100 V peak rf voltage [case (5)]. The calculated curve (straight line) corresponds to the time averaged electron density of Fig. 5(a). The experimental results correspond to the Langmuir probe measurements of the time averaged electron (●) and ion (○) density [3].

The effect of the discharge parameters and reactor geometry on the radial distribution of ion current on the powered electrode is illustrated in Figs. 12 and 13. Note that in all cases the ion current density on the powered electrode increases sharply on the very edge of the electrode. This is due to the presence of the guard ring, which imposes a zero potential very close to the driven electrode.

We see, as in the discussion on plasma density nonuniformity above, that increasing the voltage tends to enhance the nonuniformity of ion current density on the powered electrode [Fig. 12(a)]. The effect of pressure [Fig. 12(b)] is less clear. However, increasing the gap length has a strong effect on the profile of ion current density, as seen in Fig. 12(c). The ion current distribution is nonuniform and increases radially for short gap lengths [cases (7) and (1)]. When the electrode spacing is increased, the ion current distribution becomes more uniform. The ion current even slightly decreases on the edge of the electrode for the longest gap length considered [case (9)]. The ion current distribution on the driven electrode is also more uniform when the radius of the electrode is smaller, as shown in Fig. 12(d). Finally, it is interesting to note (Fig. 13) that the ion current density on the face of the driven electrode tends to be much more uniform when the guard ring is removed and when the plate surrounding this electrode is no longer grounded

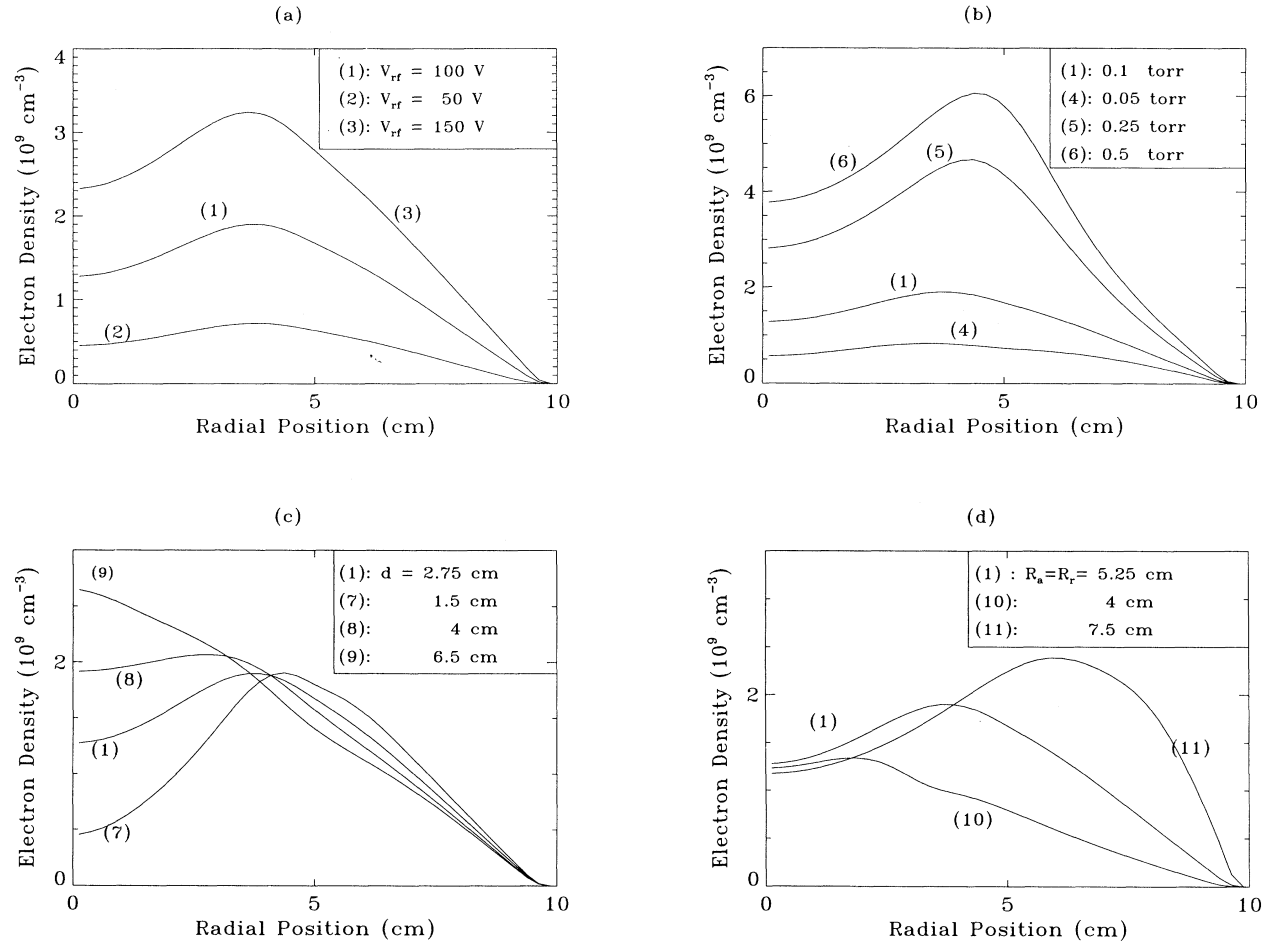

FIG. 9. Time averaged electron density as a function of radial position, for different values of (a) rf voltage V_{rf}, (b) pressure p, (c) gap length d, and (d) electrode radius R_a ($=R_r$). The corresponding case number (see Table I) is indicated on each curve. The axial position is 1.25 cm from the cathode surface, except for case (7), where it is 0.75 cm from the cathode surface (due to the short gap length in this case, 1.25 cm would be in the anode sheath; 0.75 cm corresponds to the midgap).

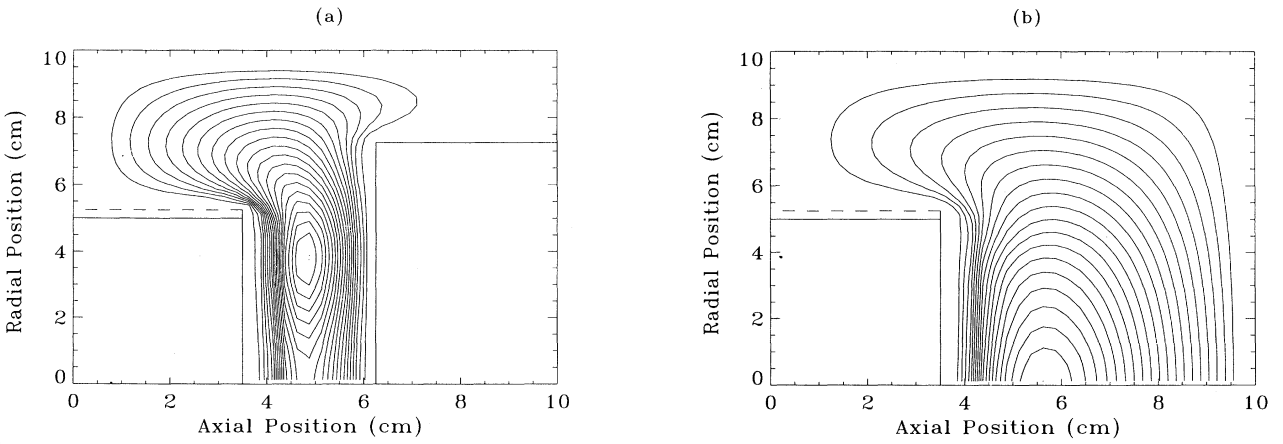

FIG. 10. Contours of constant time averaged electron number density for (a) case (12) and (b) case (9). The increment of the density contours is $\frac{1}{20}$ of the maximum density [2×10^9 cm^{-3} for (a) and 2.9×10^9 cm^{-3} for (b)].

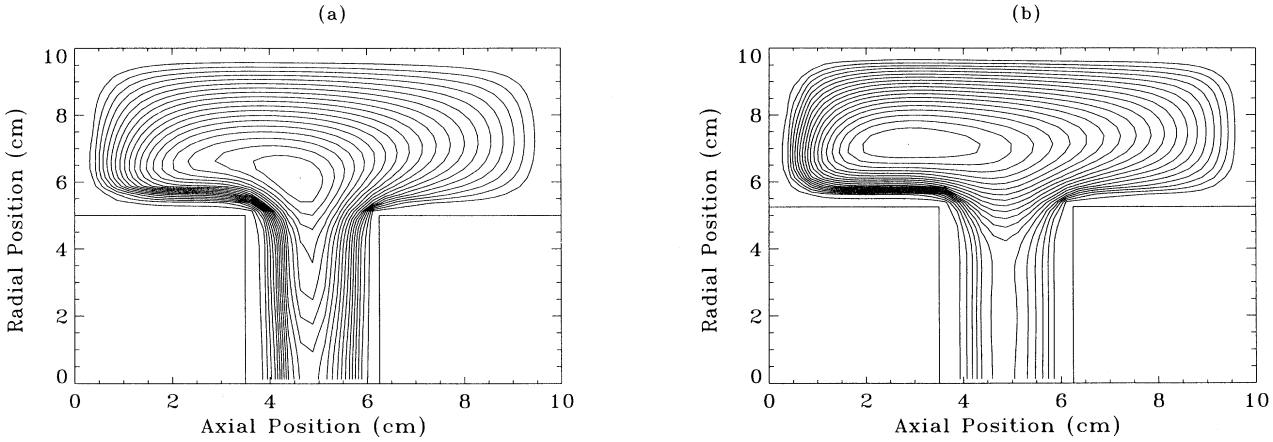

FIG. 11. Contours of constant time averaged electron number density for (a) case (13) and (b) case (14). The increment of the density contours is $\frac{1}{20}$ of the maximum density [2.05×10^{9} cm^{-3} for (a) and 3.8×10^{9} cm^{-3} for (b)].

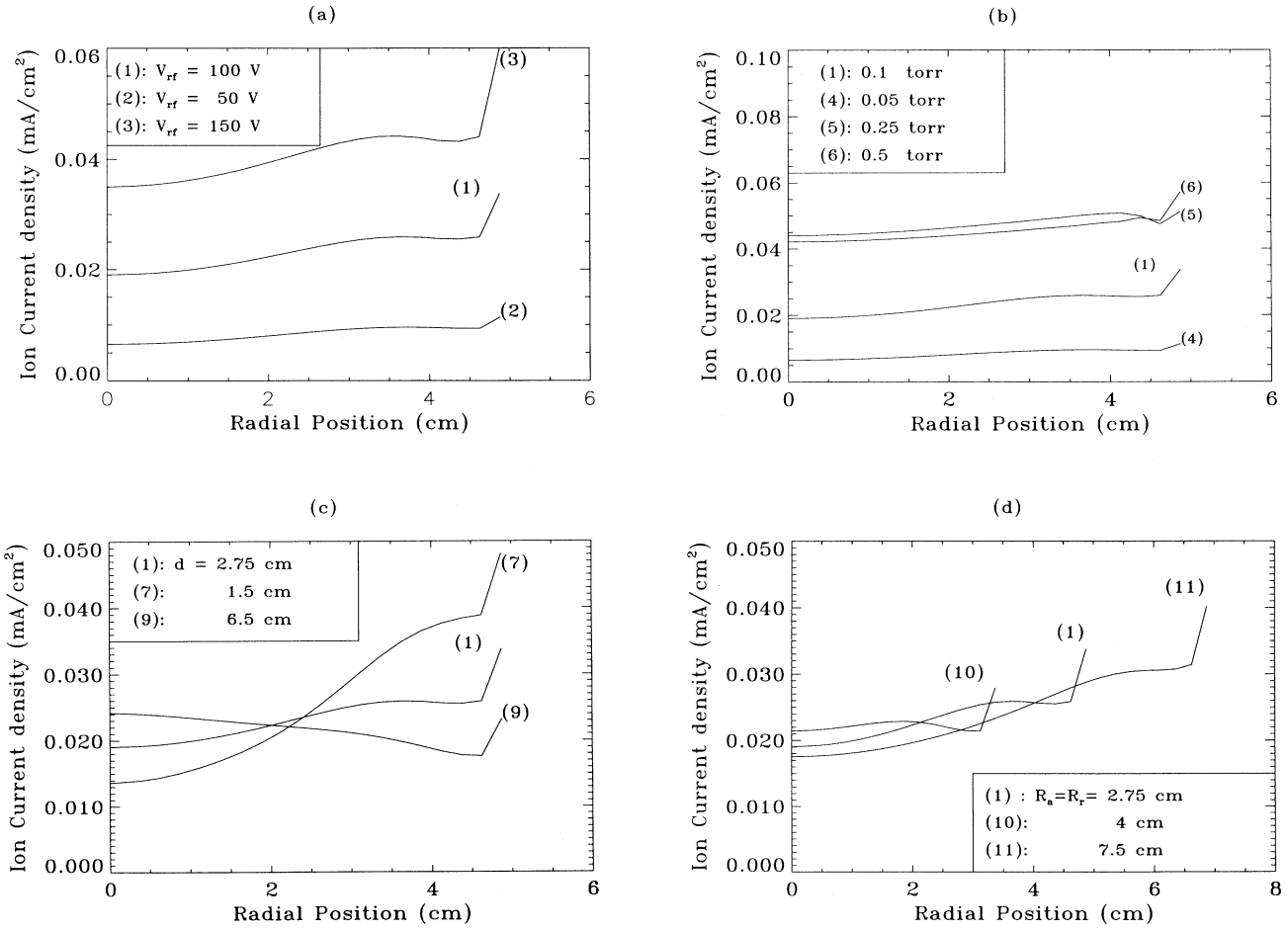

FIG. 12. Time averaged ion current density on the cathode surface as a function of radial position, for different values of (a) rf voltage V_{rf}, (b) pressure p, (c) gap length d, and (d) electrode radius R_a ($=R_r$). The corresponding case number (see Table I) is indicated on each curve.

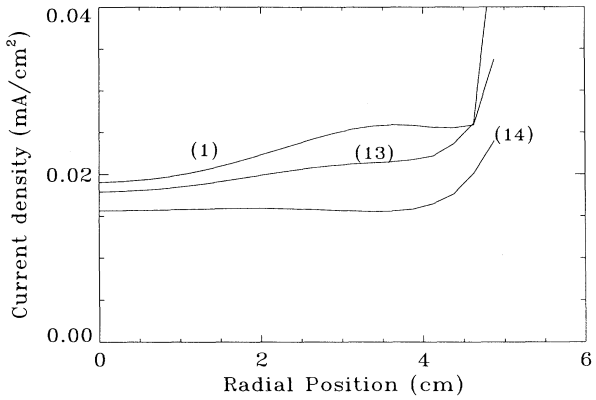

FIG. 13. Time averaged ion current density on the cathode surface for different configurations of the powered electrode. The corresponding case number (see Table I) is indicated on each curve.

TABLE II. Calculated dc self-bias, peak current, and power dissipated in the discharge for each case indicated in Table I.

	dc bias (V)	Peak current (mA)	Power (mW)
(1)	−66	136	1085
(2)	−25	55	380
(3)	−110	204	1936
(4)	−69	105	736
(5)	−59	178	2070
(6)	−53	179	2570
(7)	−64	140	1245
(8)	−66	127	969
(9)	−66	119	868
(10)	−71	66	521
(11)	−60	257	2111
(12)	−65	135	1090
(13)	−57	125	981
(14)	−34	576	3892

[cases (13) and (14)].

Overzet and Hopkins [3] suggest that the existence of the off-axis maximum of plasma density in their conditions is due to the presence of the guard ring around the driven electrode, which induces a large radial electric field on the edge of the driven electrode. The simulations tend to show that this electric field is not responsible for the off-axis maximum, because, if it were the case, this maximum would not disappear when the gap length is increased, as predicted by the model [Fig. 9(c)].

We have not found a simple analytical argument that allows us to predict whether or not the off-axis maximum between the electrodes will exist for a given set of conditions. Some ideas as to the position of the density maximum may be suggested from the following simple model calculations. We have solved the ambipolar equation for the plasma density, $-D_a \nabla n = n\nu_i$, assuming an ionization frequency of the form $\nu_i(x,\rho)=\lambda f(x,\rho)$, where λ is a parameter to be determined (eigenvalue problem) and $f(x,\rho)$ a given 2D profile. The results show that if the ionization frequency is nonzero only in the volume between the faces of the electrodes and decreasing with distance from the axis, the density maximum is on axis. Either a slight radial increase or a finite value of the ionization frequency outside the volume between the electrode faces is a necessary condition for the existence of the off-axis maximum. As the electrode separation increases, the density maximum moves closer toward the axis.

C. Peak current, power, and dc self-bias

The peak current, the discharge power, and the dc self-bias of the driven electrode for the cases of Table I are reported in Table II. We see that the dc self-bias (absolute value) increases with increasing rf voltage and decreases with increasing pressure, in qualitative agreement with the well known properties of capacitively coupled

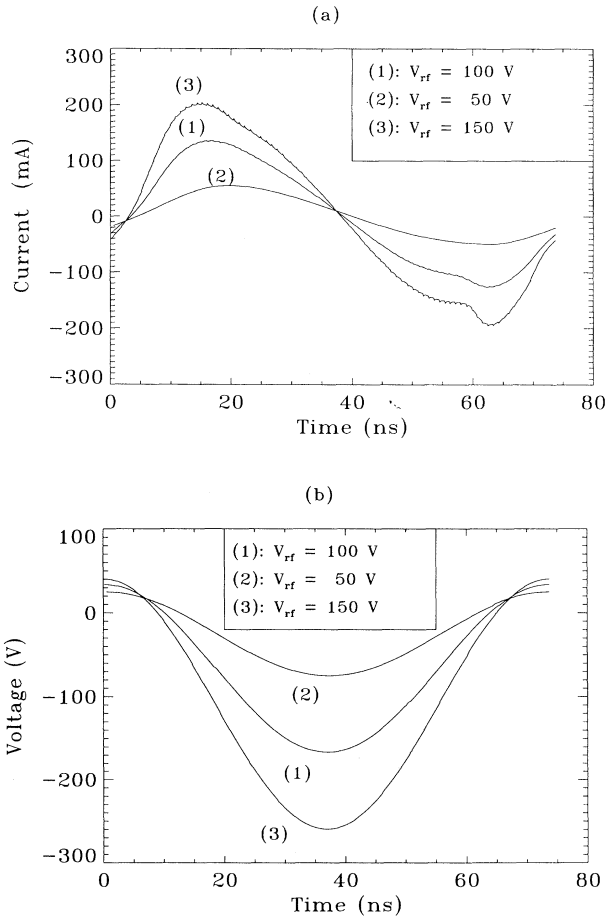

FIG. 14. Time variations during one rf cycle of (a) discharge current and (b) left electrode voltage for three different values of the rf voltage. The corresponding case number (see Table I) is indicated on each curve.

discharges. Changes in the electrode spacing have a relatively small effect on the dc bias in our conditions. The dc bias is enhanced when the driven electrode radius is decreased, as expected, since experimental results show that the dc bias is a decreasing function of the driven electrode to grounded electrode area ratio [65]. This is also why the dc bias decreases when the guard ring around the driven electrode is removed and when the plate around this electrode is no longer grounded [cases (13) and (14) of Table II, respectively]. Note in case (14) that the power dissipated in the discharge is substantially larger than in the other cases. This is because the discharge is, in that case, no longer confined between the faces of the two electrodes. Although we have seen in Sec. IV B above that the ion current density to the face of the left electrode has a good uniformity in that case, it is clear that processing in these conditions would not be very efficient.

D. Harmonic content of the total current

Figures 14(a) and 14(b) show the variations of the total discharge current and driven electrode voltage as a function of time during one rf cycle for three different values of the rf voltage. We see that the current is not perfectly sinusoidal and that the distortion increases with increasing rf voltage. The largest deviation from a purely sinusoidal form occurs when the left electrode voltage approaches zero and becomes positive, i.e., during the beginning of the anodic part of the cycle for the driven electrode. The dc self-bias of the driven electrode appears in Fig. 14(b). As expected, the dc bias increases with the amplitude of the applied rf voltage.

A systematic study of the current distortion and of the influence of the geometry on the harmonic content of the current is left to a future work.

V. CONCLUSION

The results presented in this paper can be briefly summarized as follows.

The 2D, three moment electron, two moment ion, fluid model of rf glow discharges described in this paper can well reproduce qualitatively and quantitatively the experimental measurements of plasma density distributions of Overzet and Hopkins [3] in the GEC reference cell. The model predicts an off-axis maximum of the plasma density whose location and value are very close to those measured experimentally.

The model predictions of the effect of the geometry on the discharge properties and electrical characteristics are in agreement with well known experimental observations.

We have shown how the electrode and reactor geometry, as well as the discharge parameters (pressure, rf voltage), affect (1) the existence and locations of plasma density maxima in the reactor and (2) the uniformity of the ion current to the driven electrode.

The results presented in this paper show that fluid models of rf glow discharges can be useful in helping design or improve capacitively coupled rf reactors. However, more work remains to be done to extend the validity of these models to a larger range of parameter space (e.g, to situations where the plasma chemistry modifies the electric behavior of the discharge through second kind collisions).

ACKNOWLEDGMENTS

The authors would like to thank the Joint Institute for Laboratory Astrophysics for the hospitality extended during their visit when this work was performed and for financial support for one of the authors (J.P.B). Useful discussions with R. Carlile, M. Dalvie, M. Kushner, J. O'Hanlon, and G. Selwyn are also gratefully acknowledged. This work has been supported in part by BRITE EURAM under Contract No. BE 7328.

[1] P. J. Hargis, K. E. Greenberg, P. A. Miller, J. B. Gerardo, R. A. Gottscho, A. G. Bletzinger, J. R. Roberts, J. K. Olthoff, J. R. Whetstone, R. J. Van Brunt, H. M. Anderson, M. Splichal, J. L. Mock, M. L. Passow, M. L. Brake, M. E. E. Graves, D. B. Graves, M. J. Kushner, J. T. Verdeyen, G. Selwyn, M. Dalvie, J. W. Butterbaugh, H. H. Sawin, T. R. Turner, and R. Horwath, Bull. Am. Phys. Soc. **36**, 207 (1991).

[2] L. J. Overzet and M. B. Hopkins, J. Appl. Phys. **74**, 4323 (1993).

[3] L. J. Overzet and M. B. Hopkins, Appl. Phys. Lett. **63**, 2484 (1993).

[4] A. L. Ward, Phys. Rev. A **112**, 1852 (1958).

[5] A. L. Ward, J. Appl. Phys. **33**, 2789 (1962).

[6] D. B. Graves and K. F. Jensen, IEEE Trans. Plasma Sci. **PS-14**, 78 (1986).

[7] J. P. Boeuf, Phys. Rev. A **36**, 2782 (1987).

[8] D. B. Graves, J. Appl. Phys. **62**, 88 (1987).

[9] A. D. Richards, B. E. Thompson, and H. H. Sawin, Appl. Phys. Lett. **50**, 492 (1987).

[10] M. S. Barnes, T. J. Colter, and M. E. Elta, J. Comput. Phys. **77**, 53 (1988).

[11] E. Gogolides, J. P. Nicolai, and H. H. Sawin, J. Vac. Sci. Technol. A **7**, 1001 (1989).

[12] K. Okazaki, T. Makabe, and Y. Yamaguchi, Appl. Phys. Lett. **54**, 1742 (1989).

[13] J. P. Boeuf and Ph. Belenguer, in *Nonequilibrium Processes in Partially Ionized Gases,* Vol. 220 of *NATO Advanced Study Institute Series B: Physics,* edited by M. Capitelli and J. N. Bardsley (Plenum, New York, 1990), p. 155.

[14] Ph. Belenguer and J. P. Boeuf, Phys. Rev. A **41**, 4447 (1990).

[15] M. Surrendra, D. B. Graves, and G. McJellum, Phys. Rev. A **41**, 1112 (1990).

[16] Y. H. Oh, N. H. Choi, and D. I. Choi, J. Appl. Phys. **67**, 3264 (1990).

[17] M. Meyyappan and J. P. Kreskovsky, J. Appl. Phys. **68**, 1506 (1990).

[18] S. K. Park and D. J. Economou, J. Appl. Phys. **68**, 3904 (1990).

[19] M. Meyyappan and T. R. Govindan, IEEE Trans. Plasma Sci. **PS-19**, 122 (1991).

[20] M. Surrendra, D. B. Graves, and L. S. Plano, J. Appl. Phys. **71**, 5189 (1992).

[21] T. Makabe, N. Nakano, and Y. Yamagushi, Phys. Rev. A **45**, 2520 (1992).
[22] E. Gogolides and H. Sawin, J. Appl. Phys. **72**, 3971 (1992); **72**, 3988 (1992).
[23] M. Meyyappan and T. R. Govindan, J. Appl. Phys. **74**, 2250 (1993).
[24] D. J. Economou and D. P. Lymberopoulos, J. Appl. Phys. **73**, 3668 (1993).
[25] G. Capriati, J. P. Boeuf, and M. Capitelli, Plasma Chem. Plasma Proc. **13**, 499 (1993).
[26] A. M. Popov, A. T. Rakhimov, and T. V. Rakhimova, Plasma Phys. Rep. **19**, 651 (1993).
[27] E. Gogolides, C. Buteau, A. Rhallabi, and G. Turban, J. Phys. D **27**, 818 (1994).
[28] N. Nakano, N. Shimura, Z. Lj. Petrovic, and T. Makabe, Phys. Rev. E **49**, 4455 (1994).
[29] J. P. Boeuf, J. Appl. Phys. **63**, 1342 (1988).
[30] J. H. Tsai and C. Wu, Phys. Rev. A **41**, 5626 (1990).
[31] S. Hashigushi, J. Vac. Sci. Technol. A **10**, 1339 (1992).
[32] J. P. Boeuf, L. C. Pitchford, A. Fiala, and Ph. Belenguer, Surf. Coat. Technol. **59**, 32 (1993).
[33] M. Dalvie, M. Surrendra, and G. S. Selwyn, Appl. Phys. Lett. **62**, 3207 (1993).
[34] F. F. Young and C. H. Wu, J. Appl. Phys. **74**, 839 (1993).
[35] J. D. Passchier and W. J. Goedheer, J. Appl. Phys. **74**, 3744 (1993); J. D. Passchier, Ph.D. thesis, University of Utrecht, 1994.
[36] J. P. Boeuf, Ph. Belenguer, and T. Hbid, Plasma Source Sci. Technol. **3**, 407 (1994).
[37] M. Dalvie, M. Surendra, G. S. Selwyn, and C. R. Guarnieri, Plasma Source Sci. Technol. **3**, 442 (1994); S. J. Choi, P. L. Ventzek, R. J. Hoekstra, and M. J. Kushner, *ibid.* **3**, 418 (1994).
[38] D. P. Lymberopoulos and D. J. Economou, Appl. Phys. Lett. **63**, 2478 (1993); J. Vac. Sci. Technol. A **12**, 1229 (1994).
[39] R. Boswell and I. J. Morey, Appl. Phys. Lett. **52**, 21 (1988).
[40] M. Surrendra, D. B. Graves, and I. J. Morey, Appl. Phys. Lett. **56**, 1022 (1990).
[41] D. Vender and R. W. Boswell, IEEE Trans. Plasma Sci. **PS-18**, 725 (1990).
[42] C. K. Birdsall, IEEE Trans. Plasma Sci. **PS-19**, 65 (1991).
[43] M. Surrendra and D. B. Graves, IEEE Trans. Plasma Sci. **PS-19**, 144 (1991).
[44] J. P. Boeuf and Ph. Belenguer, J. Appl. Phys. **71**, 4751 (1992).
[45] H. Date, K. Kitamori, and H. Tagashira, J. Phys. D **25**, 442 (1992).
[46] V. Vadehi, G. DiPeso, C. K. Birdsall, M. A. Lieberman, and T. D. Rognlien, Plasma Sources Sci. Technol. **2**, 261 (1993).
[47] V. Vadehi, C. K. Birdsall, M. A. Lieberman, G. DiPeso, and T. D. Rognlien, Plasma Sources Sci. Technol. **2**, 273 (1993).
[48] L. C. Pitchford, Ph. Belenguer, and J. P. Boeuf, *Microwave Discharges: Fundamental and Applications,* Vol. 302 of *NATO Advanced Study Institute Series B: Physics,* edited by C. M Ferreira and M. Moisan (Plenum, New York, 1993), p. 359.
[49] V. Vahedi, C. K. Birdsall, M. A. Lieberman, G. DiPeso, and T. D. Rognlien, Phys. Fluids B **5**, 2719 (1993).
[50] J. P. Boeuf and L. C. Pitchford, IEEE Trans. Plasma Science **PS-19**, 286 (1991).
[51] N. Sato and H. Tagashira, IEEE Trans. Plasma Sci. **PS-19**, 102 (1991).
[52] T. J. Sommerer and M. J. Kushner, J. Appl. Phys. **71**, 1654 (1992).
[53] A. Fiala, L. C. Pitchford, and J. P. Boeuf, Phys. Rev. E **49**, 5607 (1994).
[54] H. Debontride, J. Derouard, P. Edel, R. Romestain, N. Sadeghi, and J. P. Boeuf, Phys. Rev. A **40**, 5208 (1989).
[55] M. Surrendra, Plasma Source Sci. Technol. (to be published).
[56] Plasma Source Sci. Technology **3** (3) (1994), special issue on formation, transport, and consequences of particles in plasmas.
[57] K. Bløtekjaer, IEEE Trans. Electron. Devices **ED-17**, 38 (1970).
[58] K. Seeger, *Semiconductor Physics* (Springer-Verlag, New York, 1973).
[59] A. Ghis, E. Constant, and B. Boiziaux, J. Appl. Phys. **54**, 214 (1983).
[60] T. Shawki, G. Salmer, and O. El-Sayed, IEEE Trans. Electron. Devices **ED-37**, 21 (1990).
[61] P. Segur, M. Yousfi, and M. C. Bordage, J. Phys. D **17**, 2199 (1984).
[62] D. L. Scharfetter and H. K. Gummel, IEEE Trans. Electron. Devices **ED-16**, 64 (1969).
[63] P. L. G. Ventzek, T. J. Sommerer, R. J. Hoekstra, and M. J. Kushner, Appl. Phys. Lett. **63**, 605 (1993); P. L. G. Ventzek, R. J. Hoekstra, and M. J. Kushner, J. Vac. Sci. Technol. B **12**, 461 (1994); see also, S. Hashiguchi, Jpn. J. Appl. Phys. **32**, L138 (1993).
[64] S. Geha, R. N. Carlile, J. F. O'Hanlon, and G. S. Selwyn, J. Appl. Phys. **72**, 374 (1992); R. N. Carlile and S. Geha, *ibid.* **73**, 4785 (1993).
[65] B. Chapman, *Glow Discharge Processes* (Wiley, New York, 1989).